Continental Shelf Research 137 (2017) 72–83

Contents lists available at ScienceDirect

Continental Shelf Research

journal homepage: www.elsevier.com/locate/csr

Research papers

Modeling the finite-height behavior of offshore tidal sand ridges, a sensitivity study

Bing Yuan*, Huib E. de Swart, Carles Panadès

Institute for Marine and Atmospheric research Utrecht, Utrecht University, Princetonplein 5, 3584CC Utrecht, The Netherlands

ARTICLE INFO

Keywords:
Outer shelf
Tidal ellipticity
Critical bed shear stress for sand erosion
North Sea
Sand banks

ABSTRACT

Tidal sand ridges are large-scale bedforms with horizontal dimensions of several kilometers and heights in the order of tens of meters, which occur on outer shelves of coastal seas. In order to study the long-term evolution of these ridges, an idealized nonlinear numerical model was developed. With this tool, the sensitivity of the characteristics of these finite-height ridges, in particular, their shape and growth time, to 1D/2D configuration (topography varies in one/two horizontal dimensions), tidal ellipticity and critical bed shear stress for sand erosion was investigated. In the case of a 1D configuration, the root mean square height h_{rms} of the bedforms first grows exponentially and hereafter saturates. In the end, ridges in static equilibrium are obtained, i.e., h_{rms} remains constant. In contrast, when the configuration is 2D, ridges are found with spatially meandering crests that oscillate in time. Initially the bedforms are composed of a finite number of bottom modes. The meanders occur if bottom modes with crests normal to those of the initially preferred bedform exist, and their topographic wavenumbers are in the order of that of the preferred bedform or smaller. In addition, the vertical distance between the crest and trough levels should be larger than around 80% of the maximum water depth. Generally, the global growth time, i.e., the time at which h_{rms} stops increasing after the exponential growth stage of the bedforms, is slightly larger for a 2D than for a 1D configuration. The ridge shapes are sensitive to the tidal ellipticity, while they are hardly sensitive to the critical bed shear stress. The global growth time varies non-monotonically with the tidal ellipticity, and it increases if the critical bed shear stress is included. Comparison between the model results and field observations suggests that the model is able to simulate the gross characteristics of the Dutch Banks and the Flemish Banks in the southern North Sea and that these ridges may still be growing.

1. Introduction

In the offshore area of many shallow seas with sandy beds, patches of tidal sand ridges are observed (Off, 1963; Liu et al., 1998; Dyer and Huntley, 1999, and references therein). Tidal sand ridges have a typical spacing (mean distance between successive crests) of 5–10 km, their crests are cyclonically (5–30°) oriented with respect to the principal direction of the tidal current, and their height is in the order of 10 m. The formation time scale of tidal sand ridges is in the order of hundreds of years. Although extensive studies on the dynamics of these large-scale bedforms have been conducted (Roos et al., 2004, and references therein), the long-term nonlinear evolution of these seabed features is still not fully understood. Acquiring more knowledge about the behavior of these bedforms with a finite height is desirable for practical issues, such as assessment of the stability of underwater structures and strategic planning of marine sand mining (van Lancker et al., 2010).

It is now generally accepted that tidal sand ridges may form as a free instability of a system describing feedbacks between the sandy sea bed and the tidal currents (Blondeaux, 2001; Besio et al., 2006, and references therein). Linear stability analysis yields tidal sand ridges of which the spacing and orientation are in fair agreement with those of observed ridges. However, the analysis is restricted to bedforms with an infinitesimally small amplitude. To quantify the characteristics of these bedforms with a finite height, nonlinear models are needed. In Huthnance (1982a), besides the initial formation of tidal sand ridges, finite-height equilibrium ridges were shown to exist, but rather strong simplifications were made. In his model, the topography only varied in one horizontal direction (1D configuration), the tidal flow was modeled as a block flow (constant flood and ebb current), and the Coriolis force was neglected. Ridges only remained submerged in the case that either stirring of sand by waves, asymmetrical tidal currents or limited availability of sand (limited depth of the erodible bed) was considered. It was also shown that asymmetrical tidal currents give rise to asymmetrical equilibrium ridge profiles, and that the ridges migrate

* Corresponding author.
E-mail addresses: b.yuan@uu.nl (B. Yuan), H.E.deSwart@uu.nl (H.E. de Swart), C.PanadesGuinart@uu.nl (C. Panadès).

http://dx.doi.org/10.1016/j.csr.2017.02.007
Received 20 October 2016; Received in revised form 9 February 2017; Accepted 18 February 2017
Available online 21 February 2017

in the direction from their gentler side to their steeper side with respect to the crests.

The long-term evolution of topographies that varied in two horizontal dimensions (2D configuration) was further investigated in Huthnance (1982b). The near-parallel depth contours in the equilibrium state for an initial single bump bottom perturbation suggested that arbitrarily long straight ridges would form in an infinite sea under spatially uniform tidal forcing. Note that the same simplifications in the forcing as those in Huthnance (1982a) were used, and the equilibrium state was only obtained under the condition of limited availability of sand. Komarova and Newell (2000) found that the nonlinear interaction between tidal sand waves with crests normal to the principal current direction and different wavelengths could generate bedforms with spacings similar to those of tidal sand ridges. However, the crests of the bedforms generated from the interaction between tidal sand waves were normal to the principal current direction, which is different from that of the observed ridges. Idier and Astruc (2003) determined the saturation height of tidal sand ridges by the growth rate of the initially fastest growing bottom mode with different initial heights under steady/block flow. If the growth rate of the bottom mode with a certain height is zero, the ridge height is said to be saturated. In this way, the nonlinear interactions between bottom modes with different spacings were neglected, and the cross-sectional (normal to crests in space) ridge profiles in time could not be obtained.

In Roos et al. (2004), a nonlinear morphodynamic model was developed to simulate the cross-sectional profiles of finite-height tidal sand ridges, and stirring of sand by wind waves was parametrically accounted for. In that study, a 1D configuration and rectilinear tidal currents were assumed. Equilibrium ridges were shown to exist, and they were asymmetrical and migrated in the case of asymmetrical tidal currents. It was also found that the modeled ridge height overestimated the observed ridge height of the Dutch Banks in the southern North Sea. Tambroni and Blondeaux (2008) carried out a weakly nonlinear stability analysis to investigate the behavior of finite-height ridges. Their method is fast, but it is only applicable for tidal currents with large ellipticity ϵ (the ratio between the minor axis and the major axis of the tidal current ellipse). Many tidal sand ridges are actually observed at locations where tidal currents are close to rectilinear ($\epsilon \sim 0$), for instance, in the southern North Sea (Collins et al., 1995). Furthermore, the effect of the critical bed shear stress for sand erosion on the evolution of finite-height ridges has not been considered in the above studies, except in Tambroni and Blondeaux (2008). In Yuan et al. (2016), it was shown that including the critical bed shear stress for sand erosion significantly affects the characteristics of tidal sand ridges during their initial formation. In particular, the wavelength of tidal sand ridges decreases and the formation time scale of the ridges increases if the critical bed shear stress is accounted for. It is thus desirable to systematically explore the role of the critical bed shear stress in the long-term evolution of these ridges.

The aims of this study are twofold. The first is to quantify the differences in the characteristics of finite-height tidal sand ridges, i.e., their shape and growth time, assuming 1D and 2D configurations with unlimited sand, rectilinear tides and no critical bed shear stress for sand erosion. The second aim is to study the sensitivity of the characteristics of the finite-height ridges to elliptical tides and the critical bed shear stress for sand erosion. In addition, qualitative comparison between modeled and observed ridges in the southern North Sea will be done.

To fulfill these aims, an idealized nonlinear morphodynamic model was developed, based on the work of Caballeria et al. (2002), Garnier et al. (2006) and Yuan et al. (2016). The model describes the feedbacks between tidally forced depth-averaged currents and the sandy bed on the outer shelf. Following Roos et al. (2004), the formulation for sand transport accounts for tidal processes, as well as for the stirring of sand by wind waves. The model is idealized, i.e., an open domain with no sloping bottom is used to mimic the open shelf. There are two reasons to use an idealized model rather than other existing process-based models, e.g. Delft3D. One reason is that the latter do not allow for periodic boundary conditions while tidal sand ridges are manifestation of rhythmic bedforms, and the other reason is that those existing models require large computational effort for the long-term evolution of the ridges.

The manuscript is organized as follows. In Section 2, the morphodynamic model is introduced, followed by a description of numerical implementation, quantities for the characteristics of finite-height bedforms and experiments design. Results are presented in Section 3 and subsequently discussed in Section 4. Finally, Section 5 contains the conclusions.

2. Material and methods

2.1. Model

This study focuses on the nonlinear dynamics of offshore tidal sand ridges, hence an open domain is considered. The size of the domain is in the order of the spacing of these ridges, which is assumed to be much smaller than the wavelengths of the principal tidal waves. The assumption justifies imposing periodic boundary conditions and a time-varying horizontal pressure gradient force $\overrightarrow{F_p}$, which is spatially uniform on the scale of the domain. The force $\overrightarrow{F_p}$ drives a spatially uniform background depth-averaged tidal velocity vector $\overrightarrow{u_0}$ (Fig. 1) that exists in the absence of bottom undulations, and it obeys the momentum balance

$$\overrightarrow{F_p} = \frac{\partial \overrightarrow{u_0}}{\partial t} + f\overrightarrow{e_z} \times \overrightarrow{u_0} + \frac{\overrightarrow{\tau_{b0}}}{\rho H}, \quad \text{with } \overrightarrow{F_p} \equiv -g\nabla\zeta_0. \tag{1}$$

Here, ζ_0 is the surface variation induced by $\overrightarrow{F_p}$ without bottom undulations, g is the gravitational acceleration, and $f = 2\Omega \sin\Phi$ is the Coriolis parameter, with Ω the angular frequency of the Earth and Φ the latitude. Furthermore, $\overrightarrow{e_z}$ is a unit vector in the vertical direction, ρ is the constant water density, and H is the undisturbed water depth (Fig. 1). Note that in the cross product $\overrightarrow{e_z} \times \overrightarrow{u_0}$, vector $\overrightarrow{u_0}$ is interpreted as a three-dimensional vector with a zero vertical component, and that only the horizontal components of the cross product are considered. The bed shear stress vector $\overrightarrow{\tau_{b0}}$ is determined by $\overrightarrow{u_0}$ (for explicit formulation see Section 2.2), hence for a given $\overrightarrow{u_0}$, $\overrightarrow{F_p}$ is determined by Eq. (1). The horizontal components u_0 and v_0 of the spatially uniform background velocity $\overrightarrow{u_0}$ are specified as harmonic series,

$$u_0 = U_0 + \sum_i [a_i \cos(\omega_i t - \phi_i)\cos\varphi_i - b_i \sin(\omega_i t - \phi_i)\sin\varphi_i], \tag{2a}$$

$$v_0 = V_0 + \sum_i [a_i \cos(\omega_i t - \phi_i)\sin\varphi_i + b_i \sin(\omega_i t - \phi_i)\cos\varphi_i]. \tag{2b}$$

In these expressions, U_0 and V_0 are the horizontal components of the

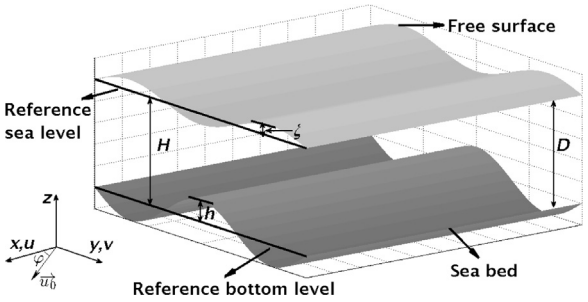

Fig. 1. Sketch of the model geometry, also showing the spatially uniform tidal velocity vector $\overrightarrow{u_0}$ in its principal direction, and the angle φ between the principal direction of the tidal current and the x-axis. Other symbols are explained in the text.

residual flow M_0, the subscript i represents different tidal constituents, with ω_i and ϕ_i being the angular frequency and phase of a tidal constituent. Furthermore, a_i and b_i are the sizes of semi-major and semi-minor axes of the tidal ellipse, and φ_i is the angle between the major axis of the tidal ellipse and the x-axis (Fig. 1). As in Hulscher et al. (1993) and Blondeaux et al. (2009), the ellipticity of the tidal constituent is defined as $\epsilon_i = b_i/a_i$. In the Northern Hemisphere, positive (negative) ϵ_i means that the end point of the velocity vector of that constituent follows an ellipse in a cyclonic (anticyclonic) sense.

In the presence of bedforms, the water motion is modeled by the depth-averaged shallow water equations:

$$\frac{\partial \widetilde{D}}{\partial t} + \nabla\cdot(\widetilde{D}\,\vec{u}) = 0, \tag{3}$$

$$\frac{\partial \vec{u}}{\partial t} + (\vec{u}\cdot\nabla)\vec{u} + f\vec{e}_z \times \vec{u} = -g\nabla\widetilde{\zeta} + \vec{F}_p - \frac{\vec{\tau}_b}{\rho\widetilde{D}}. \tag{4}$$

Here, $\widetilde{\zeta} = \zeta - \zeta_0$ is the surface elevation related to bottom undulations, where ζ is the free surface elevation, $\widetilde{D} = \widetilde{\zeta} + H - h$ is the water depth related to $\widetilde{\zeta}$, with h being the bed level with respect to the reference bottom level (Fig. 1). Vector $\vec{u}$ is the depth-averaged velocity, whose components in the x- and y-directions are u and v, respectively. Furthermore, $\vec{\tau}_b$ is the bed shear stress vector.

The bed level evolution is determined by mass conservation of sand,

$$(1-p)\frac{\partial h}{\partial t} + \nabla\cdot\langle\vec{q}\rangle = 0, \tag{5}$$

in which $\langle\cdot\rangle = T^{-1}\int_0^T \cdot\, dt$ stands for tidal average, with T the tidal period. For currents with more than one tidal constituent, the tidal period is calculated as the least common multiple of the periods of the tidal constituents. Furthermore, $\vec{q}$ is the volumetric sand transport per unit width (formulation in Section 2.2), and p is the bed porosity. Because the time scale of the bedforms considered here (order of 100 years) is much larger than that of tides (order of 1 day), the evolution of the bedforms is to a good approximation related to the divergence of net sand transport averaged over a tidal cycle. The justification for this approximation follows from scaling arguments and the averaging theory discussed in Sanders et al. (2007). Therefore, in the computation of hydrodynamics, the bed level h is fixed in a tidal cycle.

2.2. Formulations of bed shear stress and sand transport

The bed shear stress $\vec{\tau}_b$ is related to the depth-averaged current velocity through the drag coefficient C_d by the quadratic friction law

$$\vec{\tau}_b = \rho C_d|\vec{u}|\vec{u}, \quad C_d = [2.5\ln(11\widetilde{D}/k_s)]^{-2}, \tag{6}$$

where k_s is the Nikuradse roughness that measures the roughness of the sea bed. In the presence of ripples, k_s is related to the dimensionless grain size D_*(Soulsby and Whitehouse, 2005) by

$$k_s = 202\, d\, D_*^{-0.554}, \quad D_* = \left[\frac{g(s-1)}{\nu^2}\right]^{1/3} d. \tag{7}$$

Here, s is the ratio of densities of non-cohesive sand and water, d is the median grain diameter, and ν is the kinematic viscosity of water.

For sand transport, a bed load formulation is used. Suspended load is not considered, as Besio et al. (2006) found that for coarse sand and moderate tidal current, the contribution of suspended load to the initial growth of the bedforms is negligible. The formulation for sand transport is a modified version of that of Fredsøe and Deigaard (1992):

$$\vec{q} = \alpha_e(U_e^2 - U_c^2)(1 - 0.7U_c/U_e)(\vec{u} - \Lambda U_e\nabla h)\mathcal{H}(U_e - U_c). \tag{8}$$

In this expression, α_e is the sand transport coefficient given by

$$\alpha_e = \frac{30}{\mu_d\pi C'^3}\frac{1}{(s-1)g}, \tag{9}$$

where μ_d is the dynamic friction coefficient and $C' = 2.5\ln(11\widetilde{D}/2.5d)$ is the grain-related conductance coefficient. The critical depth-averaged velocity for sand erosion U_c is obtained from

$$U_c = C'[(s-1)gd\theta_c]^{1/2}, \tag{10}$$

with θ_c being the critical Shields parameter. To calculate θ_c, an empirical relation through the dimensionless grain size D_* is used (Soulsby and Whitehouse, 1997):

$$\theta_c = \frac{0.3}{1 + 1.2D_*} + 0.055[1 - e^{-0.02D_*}]. \tag{11}$$

The modification concerns the wave stirring effect on sand transport and the slope-induced transport. The wave stirring effect on sand transport is included by using a wave averaged current U_e, given by $U_e^2 = |\vec{u}|^2 + 0.5u_w^2$, where u_w is the amplitude of the depth-dependent wave-induced near-bed orbital velocity. Following Roos et al. (2004), the velocity u_w is parameterized as

$$u_w = U_w\left(\frac{H}{\widetilde{D}}\right), \tag{12}$$

in which U_w represents the near-bed orbital velocity amplitude in the absence of bottom undulations. Hereafter U_w is called wave stirring coefficient as in Roos et al. (2004). Furthermore, isotropic instead of anisotropic slope-induced sand transport is employed with a bed slope coefficient Λ, which is often used for bed load transport (e.g. Bailard and Inman, 1981). Finally, the Heaviside function $\mathcal{H}$ is used to guarantee that sand transport only occurs if $U_e > U_c$.

2.3. Numerical implementation

The system (Eqs. (1)–(12)) is solved by using an explicit finite-difference numerical scheme (Caballeria et al., 2002; Garnier et al., 2006). A central second-order discretization is used in space, while an explicit fourth-order Runge-Kutta scheme is applied for time integration. Further details about the numerical scheme are given in Garnier et al. (2006) and Yuan et al. (2016). Moreover, since the morphological time scale of offshore large-scale bedforms is much larger than the time scale of tides, a morphological acceleration factor β (Roelvink, 2006) is introduced into Eq. (5) (replace $\partial h/\partial t$ by $\partial h/\partial(\beta t)$) to accelerate the morphodynamic processes.

The finite-height behavior of sand ridges is investigated by simulating the long-term evolution of bed perturbations that initially have a small amplitude in a finite domain subject to tidal forcing. Here, background tidal currents are characterized by a single angle φ between the major axes of the ellipses of the tidal constituents and the x-axis. Angle φ and domain length L_y are linked to the orientation ϑ_p of the crests with respect to the principal current direction and the wavelength λ_p of the initially fastest growing bottom mode (or the initially preferred bedform/mode). Values of ϑ_p and λ_p (or wavenumber $k_p = 2\pi/\lambda_p$) are computed a priori by applying linear stability analysis (Huthnance, 1982a) and are thus known. Negative ϑ_p means that the crests of the bedforms are rotated cyclonically with respect to the principal current direction. The chosen set-up is that $\varphi = \vartheta_p$ and $L_y = N\lambda_p$ with N an integer. This implies that the domain is chosen such that the initially preferred bedform has its crests parallel to the x-axis and it fits into the domain. Regarding the domain length in the x-direction L_x, three grid points (two are boundary points) are used in the case of a 1D configuration, i.e., $L_x = 3\Delta x$, with Δx being the grid size in the x-direction. Regarding a 2D configuration, L_x is chosen based on a bottom mode with a wave vector $(k_{x0},\ 0)$, i.e., $L_x = 2\pi/k_{x0}$, such that $k_{x0} \simeq k_p$. As default, initially random bed perturbations are imposed with a small amplitude (approximately 0.001 H).

2.4. Quantities to describe characteristics of finite-height bedforms

The root mean square height of the bedforms $h_{rms} = (\overline{h^2})^{\frac{1}{2}}$ is used to indicate the height of the bedforms, where the overbar denotes spatial averaging $(L_x L_y)^{-1} \int_0^{L_x} \int_0^{L_y} \cdot dx\, dy$. The potential energy of the bedforms is thus measured by $h_{rms}^2/2$. The bedforms at any time contain Fourier components with wave vectors $(k_x,\ k_y) = (2\,m\pi/L_x,\ 2n\pi/L_y)$, i.e.,

$$h = \sum_m \sum_n a_{mn} e^{2\pi i(mx/L_x + ny/L_y)}. \tag{13}$$

Here, m and n are integers, $-\frac{L_x}{2\Delta x} \le m \le \frac{L_x}{2\Delta x}$, $-\frac{L_y}{2\Delta y} \le n \le \frac{L_y}{2\Delta y}$, with Δy being the grid size in the y-direction, and a_{mn} represents the complex amplitude of the corresponding component, which is obtained from inverse Fourier transform. A bottom mode consists of components with wave vectors $\pm(k_x,\ k_y)$. The potential energy of the bedforms is computed as $\sum_m \sum_n |a_{mn}|^2/2$.

To describe the growth or decay of the amplitude of the bedforms, a global growth rate Γ of the bedforms is computed (Garnier et al., 2006), which reads

$$\Gamma = \frac{1}{(h_{rms}^2)} \frac{\partial}{\partial t}\left(\frac{1}{2} h_{rms}^2\right). \tag{14}$$

A static equilibrium state of the growth of finite-height bedforms is reached if Γ remains 0, while a dynamic equilibrium state of the growth of finite-height bedforms is obtained if Γ oscillates around 0 in time. Typically, in the case of an initially random bed perturbation, Γ changes its sign after a period during which the amplitudes of the bottom modes grow exponentially. In this study, a global growth time τ_g is defined as the time when Γ turns negative after the exponential growth of the bottom modes.

In the presence of more than one tidal constituent, the bedforms could migrate and show asymmetrical profiles. To describe the cross-sectional (normal to crests) profiles of the bedforms, the relative height h_{rel} and asymmetry A defined in Roos et al. (2004) are used:

$$h_{rel} = \frac{|z_{tr}| - |z_{cr}|}{|z_{tr}|}, \quad A = \ln\left(\frac{l_1}{l_2}\right). \tag{15}$$

In these expressions, $|z_{tr}|$ and $|z_{cr}|$ are the distances between the reference sea level and the trough/crest level, and l_1 and l_2 are the horizontal distances from the crest to the neighboring troughs (Fig. 2). Recall that the crests of the initially preferred bedform are parallel to the x-axis. As most spatial variation of the bedforms is expected in the y-direction, only l_1 and l_2 along the y-axis are presented. The distances l_1 and l_2 are measured in the positive y-direction, such that $A > 0$ indicates that the steeper side with respect to the crest is in the positive y-direction when measured from the crest.

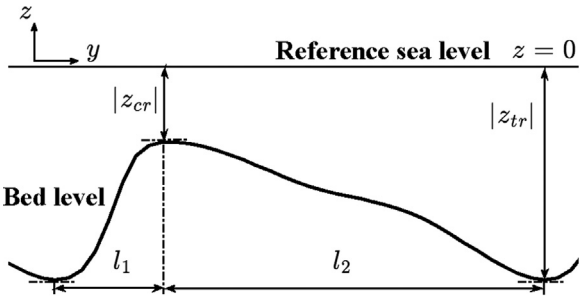

Fig. 2. Sketch showing how quantities z_{cr} and z_{tr} (crest and trough levels), and length scales l_1, l_2 are obtained from model output. From these quantities, the relative height h_{rel} and asymmetry A of the bedforms are calculated from Eq. (15). Here $A < 0$.

Table 1
Default parameter values for hydrodynamics, sand transport and numerics in the experiments. An M_2 background tidal current is considered, unless otherwise specified.

	Parameter	Value	Description
Hydrodynamics	H	30 m	Undisturbed water depth
	U_{max}	1 m s^{-1}	Maximum velocity of background tidal current
	Φ	52°N	Latitude
	Ω	7.292×10^{-5} rad s^{-1}	Angular frequency of the Earth
	g	9.81 m s^{-2}	Gravitational acceleration
	U_w	0.25 m s^{-1}	Near-bed wave stirring coefficient
	ν	1.4×10^{-6} m^2 s^{-1}	Kinematic viscosity of water
	ω_{M_2}	1.4×10^{-4} rad s^{-1}	Angular frequency of M_2 tide
Sand transport	s	2.6	Density ratio between sand and water
	p	0.4	Bed porosity
	Λ	2.0	Bed slope coefficient
	μ_d	0.6	Dynamic friction coefficient
	d	0.4 mm	Median grain size
Numerics	Δx	400 m	Grid size in the x-direction
	Δy	200 m	Grid size in the y-direction
	Δt	8 s	Time step
	β	25–450	Morphological acceleration factor

2.5. Design of experiments

To fulfill the two main aims of this study, two groups of experiments are designed. Default parameter values for hydrodynamics, sand transport and numerics are listed in Table 1. The chosen physical parameter values represent typical conditions at the outer shelf of the southern North Sea. Experiments of the first group are carried out to quantify the differences in the characteristics of finite-height tidal sand ridges, i.e., their shape and growth time, using 1D and 2D configurations under a rectilinear ($\epsilon = 0$) semidiurnal tide M_2 with no critical bed shear stress for sand erosion ($U_c = 0$).

In the second group of experiments, the focus is on exploring separately the effect of the tidal ellipticity ϵ and the critical bed shear stress, or equivalently the critical velocity U_c for sand erosion, on the characteristics of finite-height ridges. If an elliptical tidal current ($\epsilon = -0.4, -0.2, 0.2, 0.4$) is used, $U_c = 0$, while if the critical shear stress is included, $\epsilon = 0$. The values of the tidal ellipticity and the grain size in this study are based on the reconstructed tidal currents from the results of a numerical model and field data that are both presented in van Santen et al. (2011).

Accounting for the subharmonics of the initially preferred bedform, i.e., modes with wavenumbers $(0,\ k_p/I)$ (I is an integer larger than 1), increases the complexity of the system. Therefore, in Section 3 the domain length L_y is chosen as the wavelength of the initially preferred bedform. Consequently, the modes with $k_x = 0$ only include the initially preferred bedform and its superharmonics ($k = Ik_p$), as made visible as squares in Fig. 3, which is a contour plot of the initial growth rate of bottom modes in the topographic wavenumber space. Additionally, the circles in Fig. 3 denote several bottom modes with wave vectors normal/oblique to that of the preferred bedform in a 2D configuration. Simulations that include subharmonics of the preferred bedform will be discussed in Section 4.

Note that in the main part background tidal currents with multiple constituents, e.g. M_0, M_2 and its first overtide M_4 (with angular frequency $\omega_{M_4} = 2\omega_{M_2}$), are only considered when situations at specific field sites are mimicked (in Section 4). Further information of the effect of considering more than one tidal constituent on the characteristics of finite-height ridges is given in the Electronic Supplement.

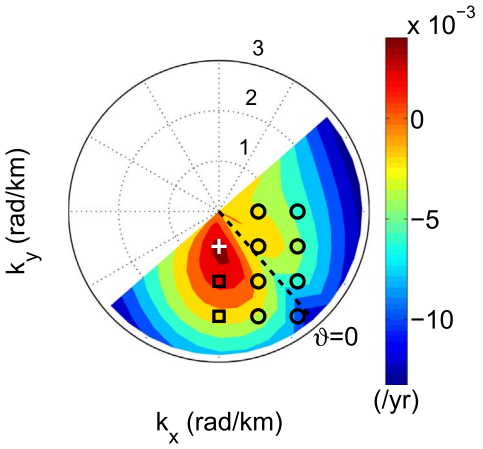

Fig. 3. An example of the initial growth rate of bottom modes as a function of the topographic wavenumbers k_x and k_y of the modes, obtained from linear stability analysis. The x- and y-axes are chosen such that the preferred bedform has a wave vector $(0,\ k_p)$. The black dashed line $\vartheta = 0$ indicates that the crests of the modes align with the principal current direction. The plus and squares correspond to the preferred bedform and two of its superharmonics, respectively. The circles denote several additional modes with crests normal/oblique to those of the preferred bedform in a 2D configuration.

3. Results

3.1. Rectilinear tides and no critical bed shear stress for sand erosion: 1D versus 2D configuration

Fig. 4 shows snapshots of the bed level h at several times in the experiments using a rectilinear M_2 background tidal current and no critical bed shear stress for sand erosion ($U_c = 0$) for both 1D and 2D configurations. Based on the wavelength and orientation of the preferred bedform, the domain length $L_y = 9$ km, and the principal current direction is 41° clockwise rotated with respect to the x-axis. In a 2D configuration, the domain length $L_x = 8$ km. Due to the selection of the bottom modes, rhythmic bottom patterns appear in both 1D and 2D cases (Fig. 4a–b). Subsequently, the crests of the bedforms reach a high level, and in the 2D case they become parallel to the x-axis (Fig. 4c). Afterwards, the change in the bed level is minor in the 1D case, while in the 2D case meandering crests appear in space (Fig. 4d). In Fig. 5 the time evolution of the bed level h of a slice along the y-direction is shown for both 1D and 2D configurations. During the first 2000 yr, the bed level evolves similarly in the two cases, while afterward it behaves quite differently. In the 1D case, after a certain time the bed level does no longer change, a result that was also found by Roos et al. (2004) (for a detailed comparison see the Electronic Supplement). In contrast, if a 2D configuration is used, after about 3000 yr the crests of the bedforms begin to oscillate in time. The oscillation of the crests has a period of roughly 300 yr, and the distance that the crests shift in the y-direction is approximately 2.4 km.

In Fig. 6, the time evolution of the root mean square height h_{rms} and the global growth rate Γ of the bedforms are shown for both 1D and 2D configurations. It is seen that for a 2D configuration, the global growth time τ_g (2500 yr) of the bedforms is larger than that in the case of a 1D configuration (1900 yr). For time $t < \tau_g$, the time evolution of h_{rms} and Γ of the bedforms is similar for the 1D and 2D configurations, although a time difference of 600 yr is observed. For t slightly larger than τ_g, the global growth rate in the 2D case starts to oscillate around 0 (dynamic equilibrium) instead of infinitely approaching 0 (static equilibrium) as in the 1D case. In the end, in the 1D case h_{rms} and the relative ridge height h_{rel} (not shown) become almost constant, whereas in the 2D case these quantities oscillate in time. The relative height of the ridges in the transect at $x = 3.2$ km in the 2D case is 87 ± 10% for time $t > \tau_g$, the mean value of which is close to that in the 1D case. As meanders could appear in the 2D case, hereafter, the results using a 2D configuration are presented, unless otherwise specified.

3.2. Elliptical tides and critical bed shear stress for sand erosion

In Fig. 7, the time series of the characteristics of the bedforms (h_{rms} and Γ) are shown for the experiments that consider M_2 background tidal currents with different values of tidal ellipticity ϵ and no critical bed shear stress for sand erosion. Results of the experiments using a 1D configuration are presented in the Electronic Supplement. The wavelength of the initially preferred bedform is largest (11.2 km) for $\epsilon = -0.4$ and smallest (8.6 km) for $\epsilon = 0.2$. The temporal behavior of Γ reveals that for all values of ϵ ($\epsilon = \pm 0.2$ not shown), similar to the case of a rectilinear tide, a dynamic equilibrium state is reached. In the case of cyclonic tidal currents ($\epsilon > 0$), for time $t > \tau_g$ the time-averaged value of h_{rms} decreases as the value of ϵ increases. In contrast, for anticyclonic tidal currents ($\epsilon < 0$), for time $t > \tau_g$ the time-averaged value of h_{rms} increases as the value of $|\epsilon|$ increases. Fig. 8a shows the dependence of the global growth time τ_g on the tidal ellipticity ϵ. Clearly, this dependence is non-monotonic, i.e, τ_g reaches a minimum at $\epsilon = -0.2$ and a maximum at $\epsilon = 0.4$. Besides, noticeable differences

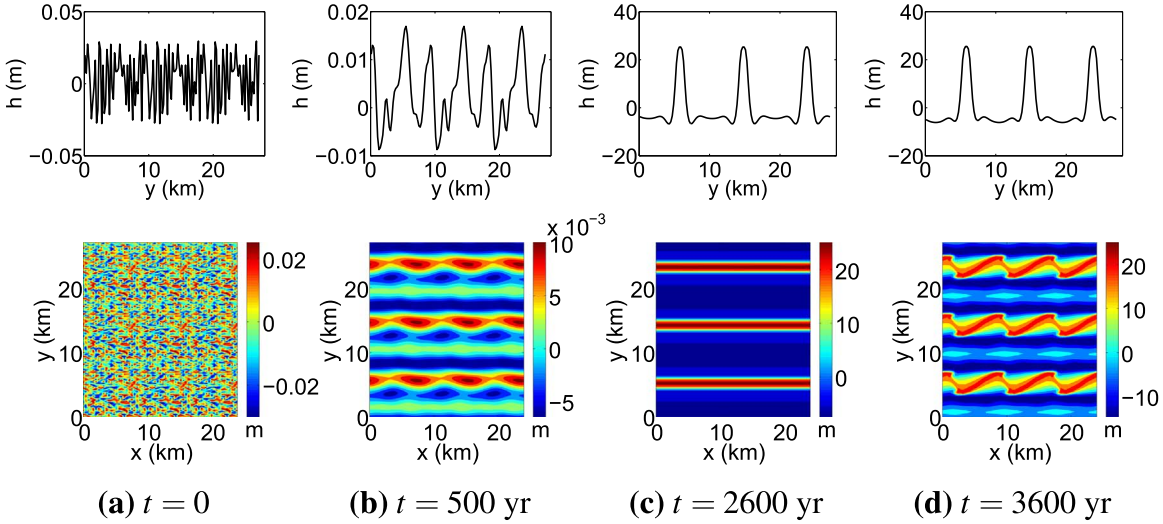

Fig. 4. Snapshots of the bed level h for both 1D (top) and 2D (bottom) configurations at times: (a) $t = 0$, (b) $t = 500$ yr, (c) $t = 2600$ yr, (d) $t = 3600$ yr, using a rectilinear M_2 background tidal current and $U_c = 0$. In the 2D case, the bed level obtained in the domain of 8 km × 9 km is used to cover a domain with a size 3 × 3 times larger. Similar extension in the y-direction is done for the 1D case.

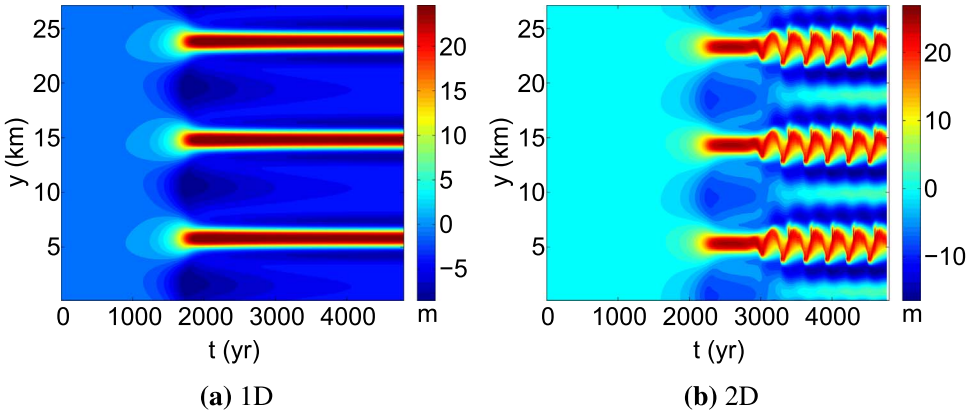

Fig. 5. Time evolution of the bed level of a slice along the y-direction in the cases using a rectilinear M_2 background tidal current and $U_c = 0$, for (a) a 1D configuration and (b) a 2D configuration. The bed level obtained in a domain with $L_y = 9$ km is used to cover a domain with L_y that is 3 times larger. In (b), $L_x = 8$ km, and the slice was taken at $x = 3.2$ km.

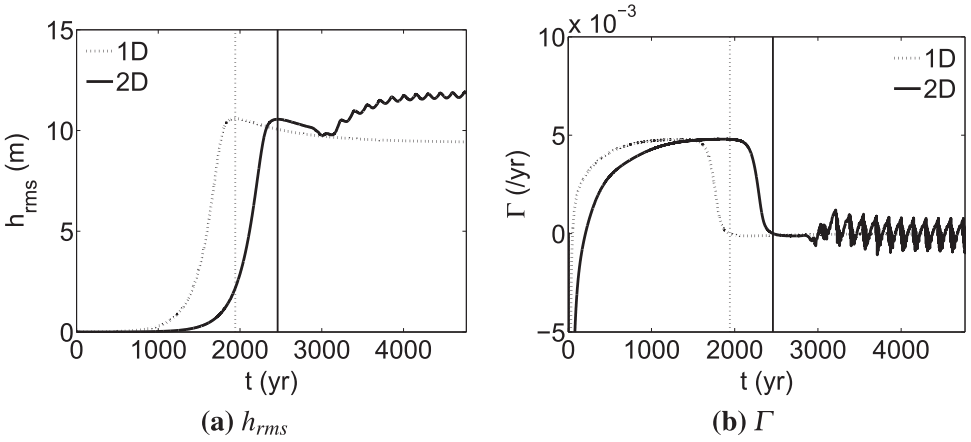

Fig. 6. Time evolution of (a) root mean square height h_{rms} and (b) global growth rate Γ of the bedforms in the cases using a rectilinear M_2 background tidal current and $U_c = 0$, for both 1D (dotted line) and 2D (solid line) configurations. The vertical lines mark the global growth time τ_g of the bedforms.

in the crest and trough levels for different values of ϵ are observed, which for each ϵ gives a large variation in the values of h_{rel}. Fig. 8b shows the range of relative ridge height h_{rel} for time $t > \tau_g$ against ϵ. For $t > \tau_g$, the maximum of h_{rel} for each ϵ is around 93%, while the minimum of h_{rel} changes from 85% at $\epsilon = -0.2$ to 48% at $\epsilon = 0.4$. Furthermore, Fig. 8c shows the period of the oscillation of the crests T_c and the distance l_c that the crests shift in the y-direction versus ϵ. It is seen that T_c increases as ϵ increases, and l_c varies between 2 km and 3.5 km. Note that l_c is larger for negative ϵ than for positive ϵ.

Next, the sensitivity of the characteristics of the bedforms to the critical velocity U_c for sand erosion is examined. In the case that $U_c > 0$, for the default value of the undisturbed water depth ($H = 30$ m, see Table 1), $U_c = 0.48$ m s^{-1}, and the initially preferred bedform has a smaller wavelength (8 km) than that (9 km) in the case that $U_c = 0$. Meandering crests that oscillate in time are also observed when $U_c > 0$ (not shown). The period of the oscillation of the crests is around 400 yr, and the distance that the crests shift in the y-direction is approximately 2.4 km. Another essential difference of the characteristics of the bedforms between the cases that $U_c = 0$ and $U_c > 0$ concerns the global growth time τ_g. In the latter case, τ_g is 500 yr larger. The other quantities (h_{rms} and h_{rel}) of the bedforms are only slightly affected if $U_c > 0$ is considered. In particular, at time $t = \tau_g$, the relative differences

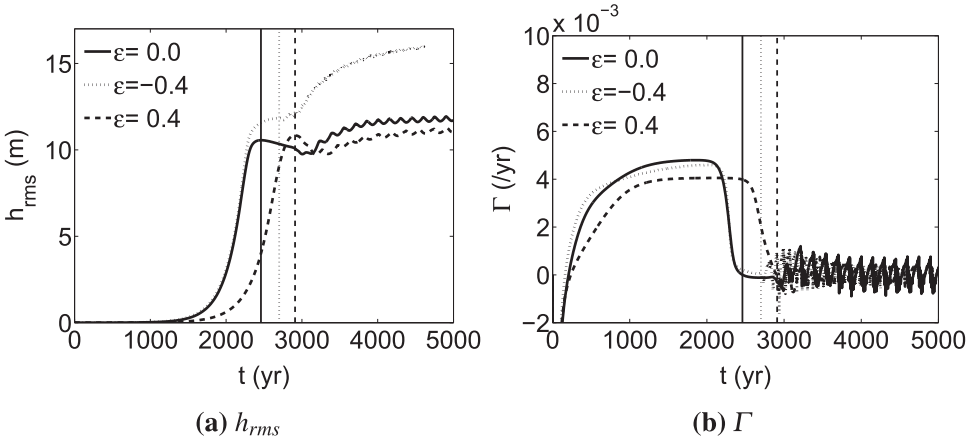

Fig. 7. As Fig. 6 but for different values of ellipticity ϵ and $U_c = 0$. The case $\epsilon = 0$ is identical to the 2D case in Fig. 6.

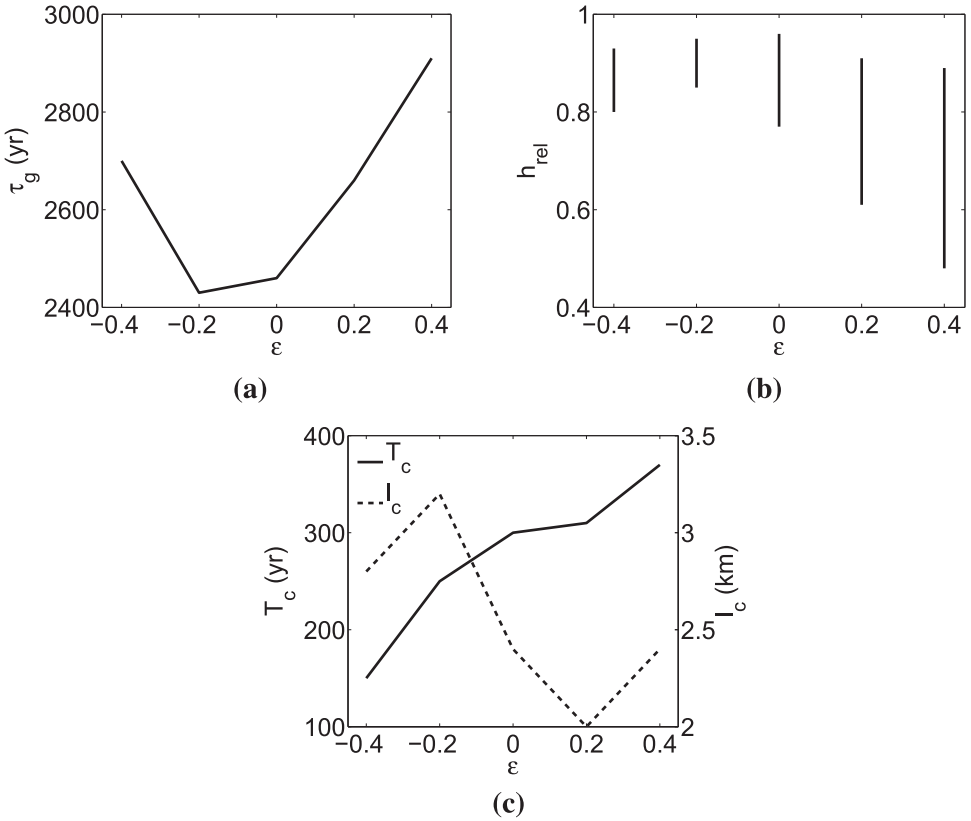

Fig. 8. (a) Global growth time τ_g versus tidal ellipticity ϵ. (b) As (a), but for relative ridge height h_{rel} in the dynamic equilibrium state ($t > \tau_g$). (c) As (b), but for the period T_c (solid line) of the oscillation of the crests and the distance l_c that the crests shift in the y-direction (dashed line).

in h_{rms} and h_{rel} between the cases that $U_c > 0$ and $U_c = 0$ are approximately 0.3% and 0.8%, respectively.

4. Discussion

4.1. Tendency of tidal sand ridges towards static equilibrium

In the experiments using a 1D configuration, finite-height tidal sand ridges in static equilibrium are obtained with the present model, i.e., the global growth rate Γ of the bedforms in the end state remains zero. In contrast, in the experiments using a 2D configuration in Section 3, ridges in dynamic equilibrium are observed, i.e., Γ oscillates in time. To further understand why tidal sand ridges in static equilibrium occur, the potential energy of the bedforms (measured by $h_{rms}^2/2$) is analyzed. From the equation of bed level evolution (Eq. (5)), the equation for the evolution of the potential energy is derived, which reads

$$\frac{\partial}{\partial t}\left(\frac{1}{2}h_{hrms}^2\right) = \frac{\overline{-h\nabla\cdot\langle\vec{q}_a\rangle}}{1-p} + \frac{\overline{-h\nabla\cdot\langle\vec{q}_s\rangle}}{1-p}. \tag{16}$$

Here, $\vec{q}_a$ and $\vec{q}_s$ are the advective and slope-induced sand transport, respectively,

$$\begin{aligned}\vec{q}_a &= \alpha_e(U_e^2 - U_c^2)(1 - 0.7U_c/U_e)\vec{u}\ \mathcal{H}(U_e - U_c),\ \vec{q}_s \\ &= \alpha_e(U_e^2 - U_c^2)(1 - 0.7U_c/U_e)(-\Lambda U_e\nabla h)\mathcal{H}(U_e - U_c).\end{aligned} \tag{17}$$

By applying the Green's theorem and periodic boundary conditions, the first and second terms on the right hand side of Eq. (16) are written as

$$\begin{aligned}P &= \frac{\overline{\langle\alpha_e(U_e^2 - U_c^2)(1 - 0.7U_c/U_e)(\nabla h\cdot\vec{u})\mathcal{H}(U_e - U_c)\rangle}}{1-p}, \\ \Delta &= -\frac{\overline{\langle\alpha_e(U_e^2 - U_c^2)(1 - 0.7U_c/U_e)\,\Lambda U_e\,\mathcal{H}(U_e - U_c)\rangle(\nabla h\cdot\nabla h)}}{1-p}.\end{aligned} \tag{18}$$

Here, P describes the production of the potential energy due to advective sand transport $\vec{q}_a$, and Δ describes the damping of the potential energy due to slope-induced sand transport $\vec{q}_s$. Note that Δ is proportional to $-\overline{\nabla h\cdot\nabla h}$, and thus its value is negative.

Fig. 9a shows the time evolution of the production and damping terms P and Δ of the potential energy and their sum in the experiment using a rectilinear M_2 background tide, critical velocity $U_c = 0$ and a 1D configuration in Section 3.1. It is seen that the balance of the production term P and the damping term Δ in the end gives rise to a state in which the potential energy of the bedforms remains constant. Initially (for time $t \lesssim 1600$ yr) the magnitudes of both P and Δ increase. At this stage, since the bed slope $|\nabla h|$ is small, the magnitude of Δ is smaller than that of P. As the potential energy increases, the bed slopes become larger, giving rise to a fast increase in Δ. The final balance between the production term P and the damping term Δ results from a more vigorous increase in Δ caused by the increasing bottom slopes, rather than by the vanishing of P. The fact that P remains positive, even for a large value of h_{rms} (see Fig. 6a), indicates that the mechanism that causes initial growth of tidal sand ridges (see Huthnance (1982a)) also persists when sand ridges have finite heights. If wind waves are present, as the near-bed wave orbital velocity amplitude is inversely proportional to the water depth, bottom erosion due to wave stirring will prevent the crest level from growing too close to the surface level. Fig. 9b shows the ridge profiles (1D configuration) in equilibrium using different values of the near-bed wave stirring coefficient U_w. It is seen that as U_w increases, the depth above the crests increases and the crests become flatter.

4.2. Presence of tidal sand ridges with meandering crests

In Section 3.1, in the case of a 2D configuration, ridges appear with meandering crests that oscillate in time. The spatial characteristics of the ridges indicate the existence of bottom modes with wave vectors in

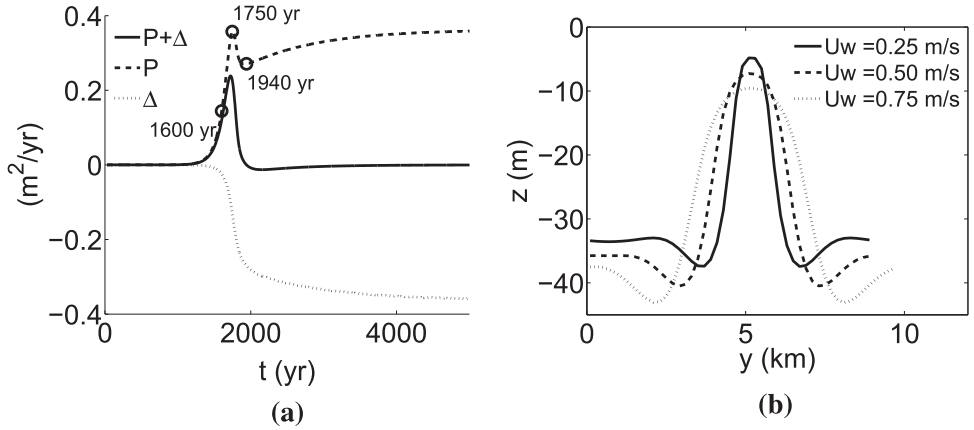

Fig. 9. (a) The production and damping terms P (dashed line) and Δ (dotted line) of the potential energy and their sum (solid line) versus time, from the experiment using a rectilinear M_2 background tidal current, $U_c = 0$ and a 1D configuration in Section 3.1. Several times are also indicated by circles. (b) Ridge profiles in equilibrium for different values of near-bed wave stirring coefficient U_w, using the same experiment setup as that for (a) except the value of U_w.

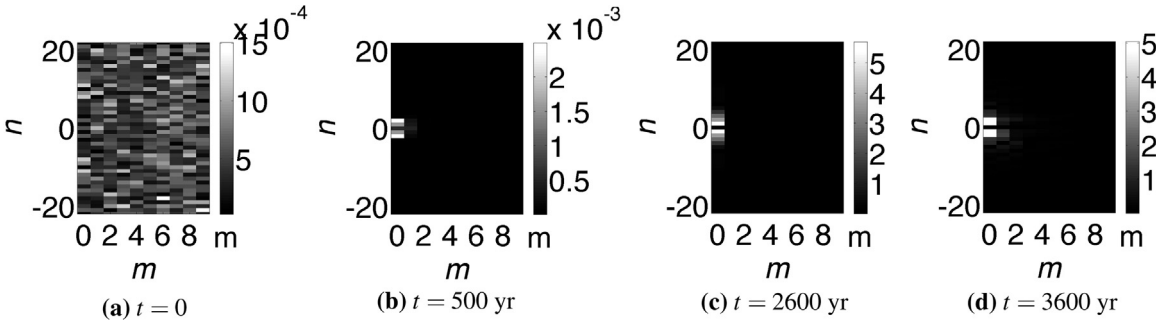

Fig. 10. Amplitude $|a_{mn}|$ of bottom modes with index (m, n) (Eq. (13)) at times: (a) $t = 0$, (b) $t = 500$ yr, (c) $t = 2600$ yr, (d) $t = 3600$ yr, corresponding to Fig. 4 (bottom). The image of $|a_{mn}|$ in the whole (m, n) space is symmetric with respect to $(0, 0)$, thus for better visualization only the part with positive m is shown. The index of the initially preferred bedform is $(0, 1)$.

different directions. To investigate this in more depth, the amplitude $|a_{mn}|$ of different bottom modes are analyzed. Fig. 10 shows the amplitude of the bottom modes at several times. It turns out that several bottom modes with crests that are oblique to those of the preferred bedform are excited at 3600 yr, which induces the meandering feature in space. Meanwhile, the temporal variations in the potential energy (measured by $|a_{mn}|^2$ for a single bottom mode) of those excited modes, the preferred bedform and its first few superharmonics cause the oscillation of the crests in time. The phenomenon that meandering crests of sand ridges evolve from straight crests is qualitatively similar to that of finite-amplitude plane waves of large steepness developing into three-dimensional (3D) crescent water waves due to nonlinear instability (Dias and Kharif, 1999, and references therein).

One mechanism that causes the evolution of water waves from a 2D to a 3D pattern is related to the growth in amplitudes of waves that have wave vectors oblique to that of the original plane wave (Toffoli et al., 2013). Similarly, the development from straight crests to meandering crests for tidal sand ridges is the result of the presence of bottom modes with crests that are oblique to those of the preferred bedform. Based on the behavior of water waves, it is hypothesized that the occurrence of meandering ridges is linked to two variables. The first is the ratio of the wavenumber of the initially preferred bedform and the minimum wavenumber of bottom modes with crests normal to those of the preferred bedform, i.e., k_p/k_{x0}. The other is the relative ridge height h_{rel}, which is strongly coupled to the near-bed wave stirring coefficient U_w. In Fig. 11a, h_{rel} at time $t = \tau_g$ is plotted against the ratio between U_w and the velocity amplitude U_{M_2} of the M_2 tide for the cases of a rectilinear M_2 background tide, $U_c = 0$ and a 2D configuration. It is seen that the larger the value of U_w/U_{M_2}, the smaller the value of h_{rel}.

Additional experiments were performed with different domain lengths L_x (recall that $k_{x0} = 2\pi/L_x$) and different values of U_w based on the experiments in Section 3. Fig. 11b shows the presence of meandering features for different values of the wavenumber ratio k_p/k_{x0} and h_{rel} at time $t = \tau_g$. In general, meanders appear if $h_{rel} \gtrsim 80\%$ and $k_p/k_{x0} \gtrsim 1$. In addition, Fig. 11c shows the period T_c of the oscillation of the crests and the distance l_c that the crests shift in the y-direction versus the wavenumber ratio k_p/k_{x0} for the cases (with different L_x) of a rectilinear M_2 tidal current and $U_c = 0$. The values of T_c and l_c increase as k_p/k_{x0} increases.

Tidal sand ridges with meandering crests are indeed observed in the field, such as the Leman Bank and the Ower Bank of the Norfolk Banks area in the southern North Sea (Caston, 1972) and the Noordhinder Bank on the Belgian Continental Shelf (Smith, 1988). In particular, Caston (1972) suggested that, possibly due to an unequal sand transport rate along the originally straight crests of the ridges, a meandering ridge grows and breaks into three ridges. Smith (1988) on the other hand examined the stability of a kink in the Noordhinder Bank over a 135 yr period and did not find support for Caston's model. Instead, Smith (1988) proposed that it is more likely that eventually the kink would break, resulting in two ridges. In the present model, breaking of a ridge into two parts indeed happens, as shown in Fig. 4c–d. Additionally, merging of two ridges (not shown) with crests almost in the same direction occurs. Thus, alternate breaking and merging of ridges in the course of time takes place.

4.3. Sensitivity of the results to numerical parameters

The sensitivity of the results to numerical settings, i.e, the morphological acceleration factor β, the time step Δt, and the grid size Δx and Δy was examined. To this end, different values of numerics were used in the experiment with a rectilinear M_2 background tidal current, $U_c = 0$ and a 2D configuration, as considered in Section 3.1. In the

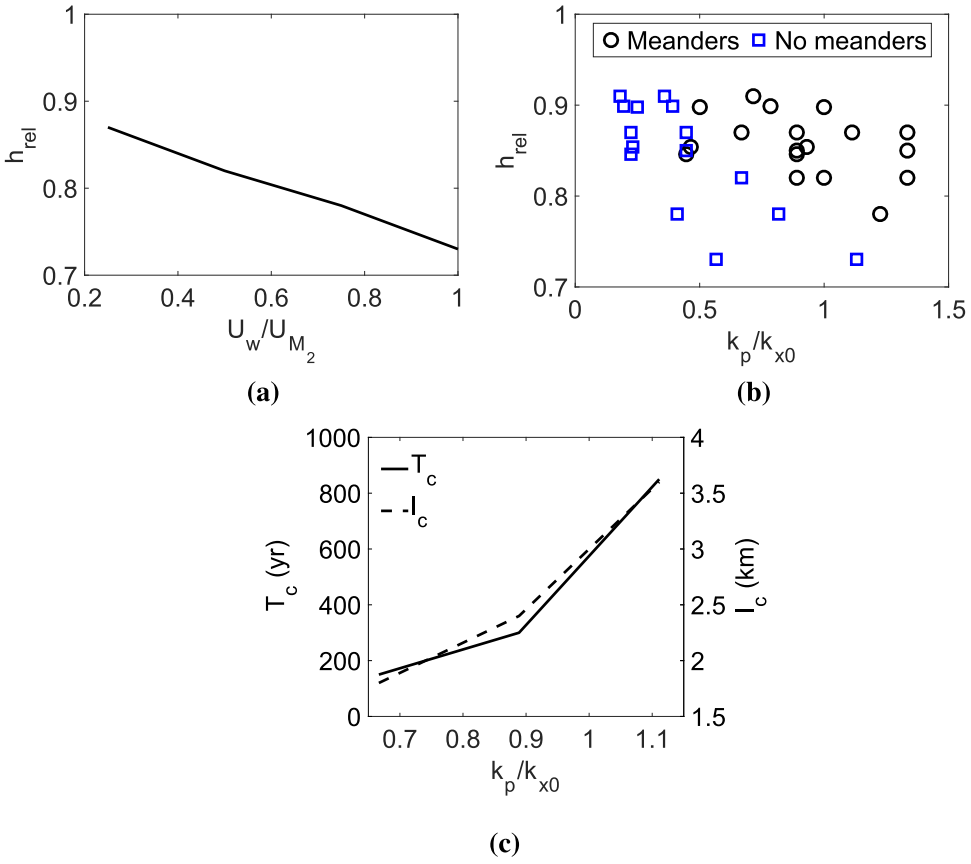

Fig. 11. (a) Relative ridge height h_{rel} at time $t = \tau_g$ (2D configuration) versus the ratio between the near-bed wave stirring coefficient U_w, and the velocity amplitude of the M_2 tide U_{M_2}. (b) Presence of meandering tidal sand ridges for different values of the wavenumber ratio k_p/k_{x0} and h_{rel} at time $t = \tau_g$, here $k_{x0} = 2\pi/L_x$ is the minimum wavenumber of the bottom modes with crests normal to those of the initially preferred bedform. (c) The period T_c (solid line) of the oscillation of the crests and the distance l_c that the crests shift in the y-direction (dashed line) versus k_p/k_{x0}. In (a) and (c), rectilinear M_2 background tidal currents were used and $U_c = 0$. For other parameters see Table 1.

reference case, $\Delta x = 400$ m, $\Delta y = 300$ m, $\Delta t = 8$ s and $\beta = 200$. For a smaller value of β, i.e., $\beta = 100$, the relative changes in the global growth time τ_g and h_{rms} at time $t = \tau_g$ of the bedforms are 0.1% and 0.02%, respectively. For a smaller time step, $\Delta t = 6$ s, the relative changes in τ_g and h_{rms} at time $t = \tau_g$ are 0.1% and 0.04%, respectively. Using a smaller grid size, $\Delta x = 200$ m and $\Delta y = 150$ m, comparing with the results in the reference case, τ_g is 0.2% larger, while h_{rms} at time $t = \tau_g$ is 2% smaller.

4.4. Role of subharmonics of the preferred bedform in the dynamics of ridges

So far, results have been presented for a domain length $L_y = \lambda_p$, such that in the direction normal to the crests of the initially preferred bedform, only the initially preferred bedform with a wavelength of λ_p and its superharmonics were included. Roos and Hulscher (2006) studied the effect of subharmonics on the finite-height sand ridges using a 1D configuration. They observed that in the presence of subharmonics of the initially preferred bedform, the average spacing between successive crests of ridges increased in time. This phenomenon, morphodynamic pattern coarsening, is observed for other types of bedforms as well, such as sand bars in the nearshore zone (Garnier et al., 2006), shoreface-connected sand ridges (Calvete and de Swart, 2003; Nnafie et al., 2014) and rippled scour depressions (Coco et al., 2007) on the inner continental shelf. In the present model, if subharmonics of the initially preferred bedform are considered, by using $L_y = I\lambda_p$ with I an integer larger than 1, coarsening of the ridges also occurs in the experiments in which no obvious meanders appear (Fig. 12a). Note that here the ridges do not migrate, and coarsening occurs as some ridges cease locally. If the bedforms migrate, merging of two parallel crests could happen due to different migration rates of the crests, as is found in the studies cited above. In contrast, if meandering ridges appear, coarsening does not take place (Fig. 12b). Hence, it seems that introducing bottom modes with crests normal/oblique to that of the initially preferred bedform inhibits the coarsening of sand ridges, due to nonlinear interactions between those modes. This may contribute to the formation of multiple ridges aligning with each other in the field (apart from breaking of a ridge into two, as suggested by Smith, 1988) since in nature bottom modes with wave vectors in all horizontal directions exist. Note that other processes can slow down the coarsening, for instance, the presence of additional background tidal constituents, such as M_0 and M_4, besides M_2 (Roos and Hulscher, 2006) and sea level rise (Nnafie et al., 2014).

4.5. Comparison between modeled and observed tidal sand ridges

Modeled tidal sand ridges are compared with two observed patches of ridges, viz. the Dutch Banks and the Flemish Banks in the southern North Sea. The observed characteristics of the ridges (after Roos et al., 2004) and the model input are listed in Table 2. The velocity amplitudes and phases of the tidal currents are based on the numerical work of van der Molen and de Swart (2001). The values of the tidal ellipticity and the grain size are adopted from van Santen et al. (2011). The modeled initially preferred bedforms have wavelengths of 6.8 km and 5.6 km for input parameters that are representative for the Dutch and Flemish Banks, respectively, which qualitatively agree with the spacings between observed ridges. The crests of the modeled ridges are approximately 40° cyclonically rotated with respect to the principal current direction. The magnitudes of the modeled orientation angles

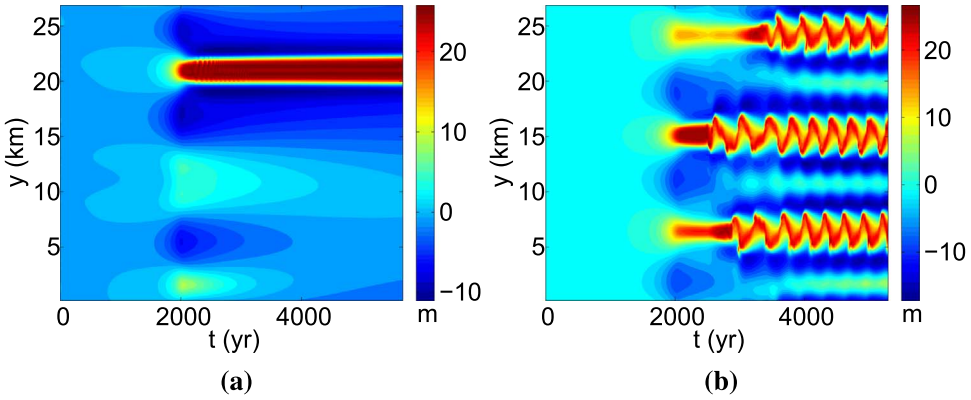

Fig. 12. Time evolution of the bed level along a slice at x = 3.2 km in the experiments with subharmonics of the preferred bedform ($L_y = 3\lambda_p$), using a rectilinear M_2 background tidal current and U_c = 0. In (a) L_x = 4 km, no obvious meanders appear; in (b) L_x = 8 km, meanders appear. For other parameters see Table 1.

Table 2
Observation at the Dutch banks and the Flemish banks and model input.

	Parameter	Dutch Banks	Flemish Banks
Observation	Latitude Ω	52°40′ N	51°30′ N
	Wavelength (km)	5.7–9.8	4.5
	Orientation ϑ (°)	−25	−6
	Relative height h_{rel} (%)	26	61
	Asymmetry A	1.3	0.2
Model input	Mean water depth H (m)	28.9	28.7
	Residual flow velocity U_{M_0} (m s^{-1})	0.01	0
	Velocity amplitude of M_2, U_{M_2} (m s^{-1})	0.69	0.74
	Velocity amplitude of M_4, U_{M_4} (m s^{-1})	0.08	0.08
	Ellipticity of M_2, ϵ_{M_2}	−0.2	0.1
	Ellipticity of M_4, ϵ_{M_4}	−0.2	0.1
	Phase of M_2, ϕ_{M_2} (°)	0	0
	Phase of M_4, ϕ_{M_4} (°)	36.4	127.5
	Grain size d (mm)	0.25	0.45

are larger than those of the observed angles.

Figs. 13 and 14 shows the observed and modeled ridge profiles for the Dutch Banks and the Flemish Banks, respectively. It is seen from Fig. 13 that the modeled ridge profiles between 6000 yr and 6500 yr (smaller than the global growth time, τ_g = 7300 yr) for the Dutch Banks are similar to the observed ridge profiles. The corresponding relative height h_{rel} (23–42%) from the modeled profiles is close to that retrieved from the field data, albeit the values of modeled and observed asymmetry A (defined in Eq. (15)) differ. The same applies to the

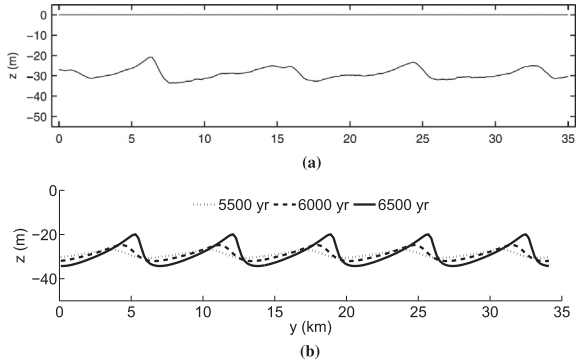

Fig. 13. (a) Observed ridge profiles in the region of the Dutch Banks in the southern North Sea (after Roos et al. (2004)). (b) Modeled ridge profiles at several times (input parameter values see Table 2). The bed level obtained in a domain with L_y = 6.8 km is used to cover a domain with L_y that is 5 times larger, and L_x = 4 km.

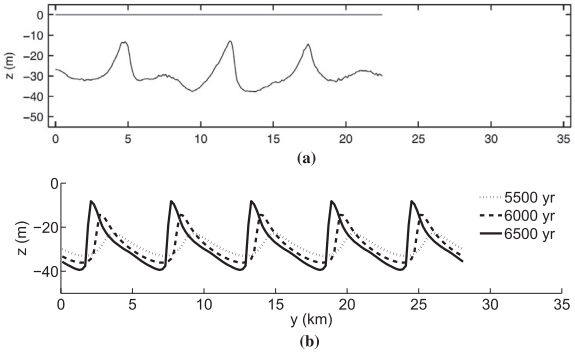

Fig. 14. As in Fig. 13 but for the Flemish Banks. In (b), the bed level obtained in a domain with L_y = 5.6 km is used to cover a domain with L_y that is 5 times larger, and L_x = 4 km.

Flemish Banks (the modeled τ_g = 6600 yr, and from 6000 yr to 6500 yr h_{rel} increases from 60% to 79%), while the location of the steeper side of the ridge with respect to the crests (indicated by the sign of A) is different from that in the field (Fig. 14). Hence, it is likely that those ridges are still growing.

There are several aspects that might explain the difference in the spacings of the modeled and observed ridges in Figs. 13 and 14. First, note that the observed spacings in Table 2 represent the dominant values obtained from Fourier analysis of the seabed topography in the regions of the Dutch Banks and the Flemish Banks. The spacing of the ridges itself in the field could vary even within a small domain as seen from Fig. 14a. Second, the background tidal forcing in the model consists of only one primary (M_2) constituent, its first overtide and the residual current, whereas in nature multiple tidal constituents are present. Third, in the model the domain size was fixed according to the spacing of the initially preferred bedform based on the present-day conditions, while in nature the spacing of the ridges could change in time due to changes in the sea level, tide and wave conditions. These aspects will be investigated in future studies.

Different location of the steeper ridge side with respect to the crests between the modeled and observed ridges (Flemish Banks setting) could be due to that the phase difference $\Delta\phi$ between the tides M_2 and M_4 used in the model is different from that in the field. In Uehara et al. (2006), it was shown that the spatial pattern of sand transport in the area of the Flemish Banks is quite complicated according to the peak bed shear stress vectors in that area, i.e., the direction of the peak bed shear stress vectors varies by 180°. Results of further experiments using different values of $\Delta\phi$ show that the magnitude and sign of A vary with $\Delta\phi$. If the tidal current consists of only M_2 and M_4, increasing/decreasing the phase difference $\Delta\phi$ between M_2 and M_4 by π changes the sign of A. This means that the new ridge profiles are like those shown in Fig. 14b, except that the steeper and gentler sides with

respect to the crests are reversed.

4.6. Limitations of the model

Several assumptions have been made in the present model. First, the vertical flow structure is neglected by employing the depth-averaged shallow water equations, so the model is unable to simulate sand waves (Hulscher, 1996). The difference between modeled and observed orientations of the bedforms could also be due to this assumption, since sand transport is determined by the near-bed currents, the direction of which may differ from that of depth averaged currents (e.g., Shapiro et al., 2004). Second, the mean sea level is assumed to be constant, while it has changed significantly over the last thousands of years. For example, it has been shown that the sea level for the continental shelves of Belgium and the Netherlands at 8 ka BP (thousands years before present) was about 15 m lower than the present sea level (Beets and van der Spek, 2000). Third, the tide and wave conditions have also changed during the last few thousands of years (Uehara et al., 2006; Neill et al., 2009), but such changes are not taken into account here. Note that no phase difference of the background tidal forcing within the study domain is considered as it is assumed that the domain size is much smaller than the wavelength of principal tidal waves, and the way of including the wind wave stirring is parametric. Additionally, only bed load transport of sand is considered, while suspended load could also play a role in the long-term evolution of these bedforms if the current is strong and the grain size is small (Besio et al., 2006). In this study, uniform grain size is assumed, while in nature multiple sand fractions are present (see e.g. Gao et al., 1994). Thus sorting processes (Walgreen et al., 2004) resulting in variation of mean grain size over the ridges are not accounted for. Last, the domain size is fixed and the principal current direction is prescribed such that the crests of the initially preferred bedform align with the x-axis. Natural selection of the wavelength and orientation of the bedforms could be possible if a 2D domain is used and its size is large enough. However, at the present stage the computational efficiency of the model hinders such kind of simulations.

5. Conclusions

Using a nonlinear morphodynamic model, the dynamics of finite-height tidal sand ridges in the shelf seas have been studied. The focus has been on the effect of considering topographies that vary in either one or two horizontal dimensions, tidal ellipticity and critical shear stress for sand erosion on shape and growth time of sand ridges.

For the range of parameter values that have been considered in this study, different results have been found between the cases using 1D and 2D configurations. Compared to the 1D case, in the 2D case it takes longer time for the ridges to reach a similar value of root mean square height h_{rms}. In the 1D case, the end state is a static equilibrium state, i.e., h_{rms} remains constant. In contrast, in the 2D case, the ridges reach a dynamic equilibrium state, if the minimum wavenumber of the bottom modes with crests normal to those of the preferred bedform is in the order or less than the wavenumber of the preferred bedform and the relative ridge height right after the global growth time is above 80%. This state is characterized by ridges with meandering crests that oscillate in time.

If elliptical tides and the critical shear stress for sand erosion are considered, tidal sand ridges with meandering crests are still observed in the 2D case. Regarding elliptical tides, noticeable changes in the shape of ridges are observed. The minimum of the relative ridge height after the global growth time varies from 85% at $\epsilon = -0.2$ to 48% at $\epsilon = 0.4$, while the maximum of the relative ridge height is around 93% for all the values of ϵ considered in this study. The global growth time of the ridges varies non-monotonically with ellipticity. In contrast, if the critical bed shear stress is considered, the ridge shape hardly changes, and the global growth time increases compared to that in the case neglecting the critical bed shear stress. The modeled ridge profiles in the period 6000–6500 yr (smaller than the global growth time) are similar to the observed ridge profiles for the Dutch Banks and the Flemish Banks in the southern North Sea. This result suggests that the ridges at those locations might still be growing.

Acknowledgements

We thank D. Calvete (Universitat Politècnica de Catalunya) and R. Garnier (Universidad de Cantabria) for assistance in setting up the model and discussions about the model results. The first author is financially supported by the China Scholarship Council (No. 201206250029).

Appendix A. Supplementary data

Supplementary data associated with this article can be found in the online version at http://dx.doi.org/10.1016/j.csr.2017.02.007.

References

Bailard, J.A., Inman, D.L., 1981. An energetics bedload model for a plane sloping beach: local transport. J. Geophys. Res. 86 (C3), 2035–2043.
Beets, D.J., van der Spek, A.J.F., 2000. The Holocene evolution of the barrier and the back-barrier basins of Belgium and the Netherlands as a function of late Weichselian morphology, relative sea-level rise and sediment supply. Geol. En. Mijnb./Neth. J. Geosci. 79 (1), 3–16.
Besio, G., Blondeaux, P., Vittori, G., 2006. On the formation of sand waves and sand banks. J. Fluid Mech. 557, 1–27.
Blondeaux, P., 2001. Mechanics of coastal forms. Annu. Rev. Fluid Mech. 33, 339–370.
Blondeaux, P., de Swart, H.E., Vittori, G., 2009. Long bed waves in tidal seas: an idealized model. J. Fluid Mech. 636, 485–495.
Caballeria, M., Coco, G., Falques, A., Huntley, D.A., 2002. Self-organization mechanisms for the formation of nearshore crescentic and transverse sand bars. J. Fluid Mech. 465, 379–410.
Calvete, D., de Swart, H.E., 2003. A nonlinear model study on the long-term behavior of shore face-connected sand ridges. J. Geophys. Res. 108 (C5), 3169. http://dx.doi.org/10.1029/2001JC001091.
Caston, V.N.D., 1972. Linear sand banks in the southern North Sea. Sedimentology 18, 63–78.
Coco, G., Murray, A.B., Green, M.O., Thieler, E.R., Hume, T.M., 2007. Sorted bed forms as self-organized patterns: 2. Complex forcing scenarios. J. Geophys. Res. 112, F03016. http://dx.doi.org/10.1029/2006JF000666.
Collins, M.B., Shimwell, S., Gao, S., Powell, H., Hewitson, C., Taylor, J.A., 1995. Water and sediment movement in the vicinity of linear sandbanks: the Norfolk Banks, southern North Sea. Mar. Geol. 123, 125–142.
Dias, F., Kharif, C., 1999. Nonlinear gravity and capillary-gravity waves. Annu. Rev. Fluid Mech. 31, 301–346.
Dyer, K.R., Huntley, D.A., 1999. The origin, classification and modelling of sand banks and ridges. Cont. Shelf Res. 19, 1285–1330.
Fredsøe, J., Deigaard, R., 1992. Mechanics of Coastal Sediment Transport. World Scientific, Singapore.
Gao, S., Collins, M.B., Lanckneus, J., Moor, G.D., Lancker, V.V., 1994. Grain size trends associated with net sediment transport patterns: an example from the Belgian continental shelf. Mar. Geol. 121, 171–185.
Garnier, R., Calvete, D., Falques, A., Caballeria, M., 2006. Generation and nonlinear evolution of shore-oblique/transverse sand bars. J. Fluid Mech. 567, 327–360.
Hulscher, S.J.M.H., 1996. Tidal-induced large-scale regular bed form patterns in a three-dimensional shallow water model. J. Geophys. Res. 101 (C9), 20727–20744.
Hulscher, S.J.M.H., de Swart, H.E., de Vriend, H.J., 1993. The generation of offshore tidal sand banks and sand waves. Cont. Shelf Res. 13 (11), 1183–1204.
Huthnance, J.M., 1982a. On one mechanism forming linear sand banks. Estuar. Coast. Shelf Sci. 14, 79–99.
Huthnance, J.M., 1982b. On the formation of sand banks of finite extent. Estuar. Coast. Shelf Sci. 15, 277–299.
Idier, D., Astruc, D., 2003. Analytical and numerical modeling of sandbanks dynamics. J. Geophys. Res. 108 (C3), 3060. http://dx.doi.org/10.1029/2001JC001205.
Komarova, N.L., Newell, A.C., 2000. Nonlinear dynamics of sand banks and sand waves. J. Fluid Mech. 415, 285–321.
Liu, Z., Xia, D., Berne, S., Wang, K., Marsset, T., Tang, Y., Bourillet, J., 1998. Tidal deposition systems of China's continental shelf, with special reference to the eastern Bohai Sea. Mar. Geol. 145, 225–253.
Neill, S.P., Scourse, J.D., Bigg, G.R., Uehara, K., 2009. Changes in wave climate over the northwest european shelf seas during the last 12,000 years. J. Geophys. Res. 114, C06015. http://dx.doi.org/10.1029/2009JC005288.
Nnafie, A., de Swart, H.E., Calvete, D., Garnier, R., 2014. Effects of sea level rise on the formation and drowning of shoreface-connected sand ridges, a model study. Cont. Shelf Res. 80, 32–48.
Off, T., 1963. Rhythmic linear sand bodies caused by tidal currents. Bull. Am. Assoc. Pet.

Geol. 47, 324–341.
Roelvink, J.A., 2006. Coastal morphodynamic evolution techniques. Coast. Eng. 53, 277–287.
Roos, P.C., Hulscher, S.J.M.H., 2006. Nonlinear modeling of tidal sandbanks: wavelength evolution and sand extraction. In: Smith, J.M. (Ed.), Proceedings of the 30th International Conference on Coastal Engineering (ICCE2006), San Diego, US, pp. 2761–2771.
Roos, P.C., Hulscher, S.J.M.H., Knaapen, M.A.F., 2004. The cross-sectional shape of tidal sandbanks: modelling and observation. J. Geophys. Res. 109, F02003.
Sanders, J.A., Verhulst, F., Murdock, J., 2007. Averaging Methods in Nonlinear Dynamical Systems 2nd edition. Springer Science & Business Media.
Shapiro, G.I., van der Molen, J., de Swart, H.E., 2004. The effect of velocity veering on sand transport in a shallow sea. Ocean Dyn. 54, 415–423.
Smith, D.B., 1988. Stability of an offset kink in the North Hinder Bank. In: De Boer, P.L., Van Gelder, A., Nio, S.D. (Eds.), Tide-Influenced Sedimentary Environments and Facies. D. Reidel Publishing Company, Dordrecht, 65–78.
Soulsby, R.L., Whitehouse, R.J.S., 1997. Threshold of sediment motion in coastal environments. In: Proceedings Pacific Coasts and Ports 1997 Conference, Christchurch, University of Canterbury, New Zealand, Wallingford, pp. 149–154.
Soulsby, R.L., Whitehouse, R.J.S., 2005. Prediction of ripple properties in shelf seas. Mark 2 predictor for time evolution. Tech. Rep. TR155 Release 2.0, HR Wallingford Ltd, UK.
Tambroni, N., Blondeaux, P., 2008. Sand banks of finite amplitude. J. Geophys. Res. 113, C10028. http://dx.doi.org/10.1029/2007JC004658.
Toffoli, A., Fernandez, L., Monbaliu, J., Benoit, M., Gagnaire-Renou, E., Lefevre, J.M., Cavaleri, L., Proment, D., Pakozdi, C., Stansberg, C.T., Waseda, T., Onorato, M., 2013. Experimental evidence of the modulation of a plane wave to oblique perturbations and generation of rogue waves in finite water depth. Phys. Fluids 25, 090701.
Uehara, K., Scourse, J.D., Horsburgh, K.J., Lambeck, K., Purcell, A.P., 2006. Tidal evolution of the northwest European shelf seas from the Last Glacial Maximum to the present. J. Geophys. Res. 111, C09025. http://dx.doi.org/10.1029/2006JC003531.
van der Molen, J., de Swart, H.E., 2001. Holocene tidal conditions and tide-induced sand transport in the southern North Sea. J. Geophys. Res. 106 (C5), 9339–9362.
van Lancker, V.R., Bonne, W., Garel, E., Degrendele, K., Roche, M., den Eynde, D.V., Bellec, V., Brière, C., Collins, M.B., Velegrakis, A.F., 2010. Recommendations for the sustainable exploitation of tidal sandbanks. J. Coast. Res. 51, 151–164.
van Santen, R.B., de Swart, H.E., van Dijk, T.A.G.P., 2011. Sensitivity of tidal sand wavelength to environmental parameters: a combined data analysis and modelling approach. Cont. Shelf Res. 31, 966–978.
Walgreen, M., de Swart, H.E., Calvete, D., 2004. A model for grain-size sorting over tidal sand ridges. Ocean Dyn. 54, 374–384.
Yuan, B., de Swart, H.E., Panadès, C., 2016. Sensitivity of growth characteristics of tidal sand ridges and long bed waves to formulations of bed shear stress, sand transport and tidal forcing: a numerical model study. Cont. Shelf Res. 127, 28–42.